

Adsorbed oxygen dynamics at forced convection interface in the oxygen evolution reaction

Received: 24 January 2025

Accepted: 13 August 2025

Published online: 26 August 2025

 Check for updatesZhixuan Chen , Ze Lin , Xiaoyu Zhu, Yahui Li & Ying Wang ✉

The oxygen evolution reaction is a prevalent anodic reaction in electrocatalytic processes. Modulation of adsorbed oxygen (*O) at the electrochemical interface is an effective means to reduce the overpotential of the oxygen evolution reaction. However, the contribution of various *O conversions to the overpotential remains unclear. Herein, the development of a multi-component forced convection electrochemical mass spectrometry constructs *O-labeled electrochemical interfaces with specific coverages to track the *O conversions. The relationships between the Faradic contributions and the specific *O conversion pathways are established by considering the anomalous fractionation of molecule oxygen. Our experiments confirm that *O coupling contributes up to 48% with a specific overpotential on full coverage platinum. Distinguishing the *O conversion contributions with various coverages reveals that balancing the *O formation and conversions, especially *O coupling enables further minimization of the overpotential of the oxygen evolution reaction. Thus, tracking the intermediate conversions has implications for designing high-performance electrocatalytic interfaces.

The oxygen evolution reaction (OER) is the most prevalent anodic reaction for providing protons and electrons in electrocatalytic processes such as hydrogen evolution or CO₂ reduction^{1,2}. However, it often becomes a limiting step in electrochemical devices owing to the involvement of multiple intermediates with high energy barriers, leading to great overpotentials³. Therefore, regulating the core intermediates on electrochemical interfaces opens an opportunity for performance improvement, providing high efficiency and low energy consumption⁴. As a fork that yields various coupling products, adsorbed oxygen (*O) is the key intermediate in determining the OER overpotential^{5,6}. It is reported that *O can be oxidized by H₂O to form *OOH (*O–OH), known as the adsorbate evolution mechanism (AEM), or directly coupled at specific interfaces (*O–O*), referred to as the oxide path mechanism (OPM)^{7,8}. The theoretical limit of the OER overpotential involving only AEM is revealed to be at 370 ± 100 mV⁹. While the emerging OPM is recognized as critical for reducing the overpotential to below 200 mV (Fig. 1a)¹⁰. The coexistence of

various *O conversions makes clarifying the relationships between them and overpotentials critical for designing high-performance OER interfaces.

Detection of adsorbed species by in situ spectroscopic techniques provided the first evidence of the specific *O conversion process^{5,11,12}. For example, comparison between the products of *O–OH and *O–O* (*OOH and *OO*, respectively) demonstrated that OPM led to lower overpotentials^{8,13}. Although it is possible to directly monitor the conversions of *O, the time resolution is sacrificed to obtain signals from trace intermediates, resulting in a minimum sampling interval of only 0.1 V. Revealing the specific overpotentials of different *O conversions requires the development of in situ techniques with higher temporal resolution¹⁴. Moreover, uncertainties in molecular adsorption states, electrode surface properties, and local reaction microenvironments all invalidate the Lambert-Beer law. The lack of a quantitative relationship between signal intensity and Faradaic current prevents the assessment of overpotential composition in complex OER processes.

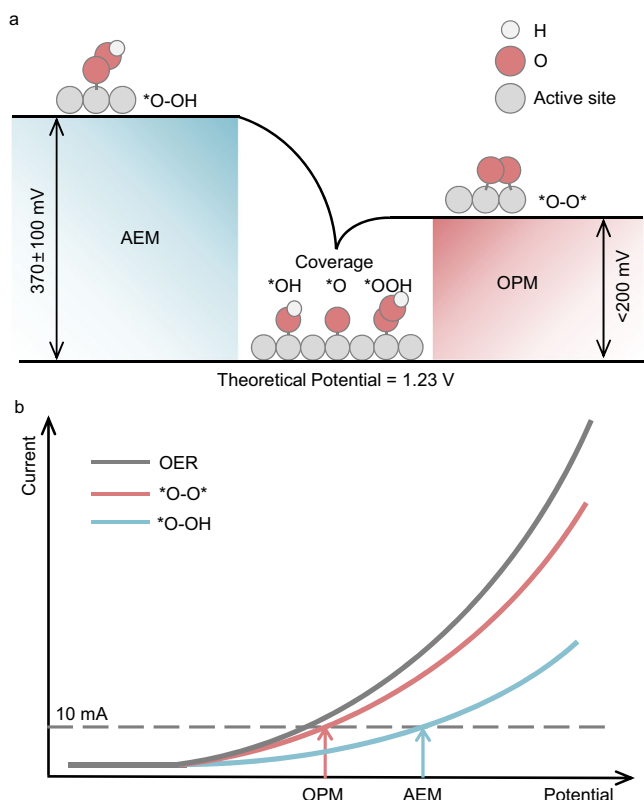


Fig. 1 | Revealing $\ast\text{O}$ conversions by MFC-MS. **a** Schematic of revealing $\ast\text{O}$ conversions leading to different overpotentials by modulation of $\ast\text{O}$ coverage. The cyan and red shading represent the overpotential of the adsorbate evolution mechanism (AEM) and the oxide path mechanism (OPM), respectively; **b** Anatomy of the OER overpotential contributions based on $\ast\text{O}$ conversions.

Isotopic labeling has emerged as an effective approach to trace the origin of products. In situ characterization techniques incorporating isotope labeling have become an effective approach for tracing the origin of products^{15,16}. Oxygen isotope labeling has an irreplaceable role in understanding the mechanism of electrocatalytic reactions involving oxygen^{17,18}. By establishing a linear relationship between the MS intensity of products and the Faradaic current, the partial currents obtained help elucidate the relative contributions of different intermediate conversions to the overpotential¹⁹. Through resolving the overall Faradaic current, the modulating effect of the interfacial microenvironment on the two competing reactions can be revealed²⁰. Recently, it has been reported that the design of active site spacing can enhance the ability of $\ast\text{O}-\text{O}^\ast$ to significantly reduce the OER overpotential²¹. However, uncertainty in the interfacial abundance makes it difficult to correlate each type of $\ast\text{O}$ conversion with the MS signal. Specifically, $\ast\text{O}$ is highly susceptible to redox and even desorption under the steady state, causing uncontrollable $\ast\text{O}$ coverage²². Furthermore, the abundance of labeled $\ast\text{O}$ at low-coverage is easily disturbed by subsequent water cleavage in OER, and thus the given partial currents of specific O_2 may not be fully equivalent to $\ast\text{O}$ conversions. In contrast, the high coverage of $\ast\text{O}$ increases its intrinsic generation barrier and exceeds that of oxidation, thereby ensuring that the OER products are exclusively derived from previously labeled $\ast\text{O}$ ²³. The transfer of $\ast\text{O}$ -labeled interfaces with specific coverages to natural abundance is expected to establish a relationship between $\ast\text{O}$ conversions and OER currents²⁴. Forced convection is one of the most effective means to transport target molecules to the active site while maintaining interfacial homogeneity^{25,26}. Therefore, delivering water molecules with different abundances to high-coverage $\ast\text{O}$ interfaces by

forced convection allows to elucidate the specific overpotentials and relative contributions of various $\ast\text{O}$ conversions.

Herein, a one-of-its-kind multi-component forced convection electrochemical mass spectrometry (MFC-MS) is developed. A stable laminar flow is constructed at the electrode interface using microfluidic technology, which enables accurate control of oxygen isotope abundance under steady state. In combination with stripping-like voltammetry, specific coverages of $\ast\text{O}$ are isotopically labeled under a constant potential and stripped via $\ast\text{O}-\text{O}^\ast$ or $\ast\text{O}-\text{OH}$ depending on the interfacial property. The generation of molecular oxygen produce an extraordinary fractionation and takes place at distinct onset potentials, which are monitored by in situ MS. Partial currents generated by O_2 molecules with different mass-to-charge ratios reveal the OER composition owing to the high coverage of $\ast\text{O}$ (Fig. 1b). Pt is found to have an apparent $\ast\text{O}-\text{O}^\ast$ activity, contributing up to 48% in OER. The negligible $\ast\text{O}-\text{O}^\ast$ contribution exhibited by Ru, which is consistent with previous reports, validates the feasibility of this approach. In addition, a relationship between the $\ast\text{O}$ conversion and its coverage is observed, providing insight for designing low-overpotential OER interfaces. Increasing the $\ast\text{O}$ coverage certainly strengthens $\ast\text{O}-\text{O}^\ast$ to break the linear scale relationship, but weakens the binding of $\ast\text{O}$ to the active site and thus leads to high overpotentials. Based on MFC-MS findings, a series of bimetallic interfaces where $\ast\text{O}$ formation and conversion occur in tandem are designed. The best performance among them reduces the OER overpotential to 196 mV, comparable to the best electrocatalysts currently available. Ultimately, the proposed technique is not only capable of assessing the intermediate transformations at the OER interface but also provides technical support for interface design to minimize the OER overpotential.

Results

MFC-MS construction based on the microchannel electrochemical cell for online observation of OER with forced convection

Versatile configuration integrated MFC-MS was built to observe the $\ast\text{O}$ conversions online under multi-component forced convection (Fig. 2a, and Supplementary Fig. 1). The microchannel electrochemical cell with forced convection was the core of MFC-MS for transporting water molecules to electrodes (Fig. 2b). It was manufactured by photolithography process, including bonding of single crystal silicon with quartz, spin-coating by negative photoresist, ultraviolet patterning, silicon etching and encapsulation (Fig. 2c). The manufacturing details were provided in “Methods” section. The electrochemical reaction area was confined in an extremely thin layer (500 μm), promoting a stable fluid movement. The extremely low Reynolds number of 36.25 at a flow rate of 4 cm s^{-1} confirmed the stable laminar flow at the interface, enabling control of the water molecule components by forced convection²⁷. Visualization of fluid motion in the microchannel cell by finite element simulation revealed the fluid homogeneity across the device at flow rates below 2 cm s^{-1} (Supplementary Fig. 2). Corner-generated vortices, which enlarged with increasing flow rate destabilized the electrode interface at 4 cm s^{-1} , thus defining the limit for maintaining forced convection. To achieve multi-component forced convection, electrolytes were precisely injected into the electrochemical cell using a multi-channel syringe pump equipped with a programmable logic controller (Fig. 2a). After pre-filling with electrolyte, high-resolution imaging of the simulation showed that forced convection inside the cell provided a complete exchange of water molecules within a second (Supplementary Fig. 3). Tiny electrolyte volume and directional fluidic facilitated the rapid translocation of labeled $\ast\text{O}$ to specific microenvironments at homeostasis. Pt, chosen as the model catalyst for $\ast\text{O}$ labeling and conversions due to its well-known oxygen redox region, was deposited on a polytetrafluoroethylene (PTFE) membrane via magnetron sputtering, namely Pt-mem²⁸. A capillary with negative pressure was positioned adjacent

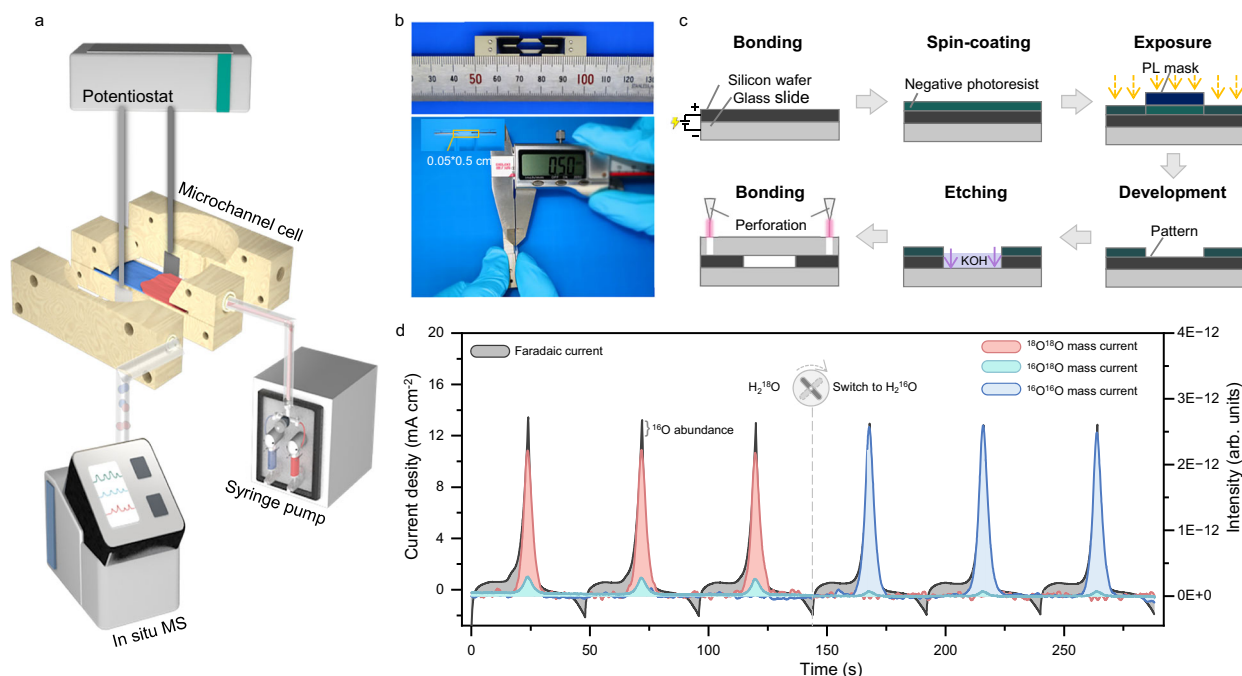


Fig. 2 | Online observation of OER under forced convection controlled by MFC-MS. **a** Schematic of the MFC-MS operation mode; **b** Images and dimensions of the microchannel electrochemical cell; **c** Schematic of the fabrication procedure of the microchannel cell; **d** CV curves and corresponding MS signals of Pt-mem in MFC-

MS accompanied by a switch with H_2^{16}O and H_2^{18}O . Reaction conditions: electrolytes 0.5 M H_2SO_4 with H_2^{16}O and H_2^{18}O ; potential range 0.4–1.8 V; scan rate 10 mV s^{-1} . The potentials applied were not iR corrected. Source data for the results are provided as a Source Data file.

to the working electrode, capturing the generated volatile species for in situ MS analysis. The voltammetric curve of Pt-mem featured recognizable redox peaks corresponding to the oxygen signals observed by MFC-MS (Supplementary Fig. 4, 5). Notably, the abundance of ^{16}O in H_2^{18}O produced a non-negligible ^{16}O behavior, in terms of the evolution of $^{34}\text{O}_2$ (Supplementary Fig. 5b). Therefore, the abundance of labeled $^*\text{O}$ must be considered when establishing the relationship between $^*\text{O}$ conversions and O_2 fractionation.

To evaluate the MFC-MS capability in controlling water molecules, six cycles of cyclic voltammetry (CV) were performed with alternating H_2^{18}O and H_2^{16}O in between (Fig. 2d). The results demonstrated that Pt-mem in MFC-MS achieved stable and reproducible OER during electrochemical scanning. Notably, after switching the fluid, the measured O_2 fractionation shifted completely from the isotopic abundance of H_2^{18}O to the natural abundance. The overpotential was maintained at ~440 mV in each cycle, with a slight elevation in H_2^{18}O . In contrast, the kinetic differences due to the greater mass of ^{18}O were more pronounced in the different electrolytes, which will be discussed in detail below. Voltammetric tests conducted at different flow rates also displayed that neither the Faradaic current nor the MS signal varied, indicating that the velocity of forced convection did not affect the electrocatalytic performance or products collection (Supplementary Fig. 6). These observations proved that the components of oxygen abundance were successfully switched while maintaining circuit integrity, demonstrating that MFC-MS could assist in labeling and tracking the $^*\text{O}$ conversions. Additionally, a linear relationship between the MS signal and the Faradaic signal was established through steady-state measurements, allowing for the partial currents of oxygen species with different mass-to-charge ratios to be extracted from the total Faradaic current (Supplementary Fig. 7)²⁰.

Isotopic labeling of oxygen species via stripping-like voltammetry to induce extraordinary fractionation of OER

In order to investigate various conversions of $^*\text{O}$, a stripping-like voltammetry procedure was applied (Fig. 3a). A high coverage of labeled $^*\text{O}$ was constructed by pre-oxidation in H_2^{18}O , which was subsequently

converted to O_2 via different pathways in H_2^{16}O . MFC-MS not only achieved the switching of oxygen abundance on the interface but also enabled the in situ analysis of O_2 fractionation during this procedure. In order to accurately obtain overpotential information, iR compensation was performed on the stripping process (Supplementary Fig. 8). Anomalous fractionation of the molecular oxygen evolution was observed by this stripping-like voltammetry and suggested that additional ^{18}O was involved in OER (Fig. 3b, and Supplementary Fig. 9). Based on the normalized partial currents, the overpotentials of $^{36}\text{O}_2$ and $^{34}\text{O}_2$ on Pt-mem were 35 and 16 mV lower than that of overall OER (440 mV), respectively. In contrast, $^{32}\text{O}_2$ generated by stripping-like voltammetry had a 42 mV higher overpotential. Clearly, the OER overpotential was composed of two conversions in this procedure. It could be hypothesized that stripping-like procedure made the OER on Pt-mem appeared to proceed in three stages: First, pre-oxidized ^{18}O underwent intermolecular coupling to form $^{36}\text{O}_2$. Then it was nucleophilic attacked by H_2^{16}O to produce $^{34}\text{O}_2$. Ultimately, water re-cleavage and additional electron transfer allowed $^{32}\text{O}_2$ to be generated at a higher overpotential.

The isotope kinetic effects (KIE) of labeled $^*\text{O}$ was the first factor which needed to be ruled out as causing similar phenomenon. Although ^{18}O theoretically exhibited a slower reaction kinetic because of larger atomic mass, anomalous KIE had also been observed on Pt^{29,30}. A comparison of the OER currents in H_2^{16}O and H_2^{18}O revealed that ^{18}O displayed a slower OER kinetic on Pt-mem (Supplementary Fig. 9a). The correction factor required to match the polarization curves for Pt-mem in both electrolytes was calculated to be 1.41 (Supplementary Fig. 9b)³¹. Applying ^{16}O for isotopic labeling similarly induced sequential OER with different mass-to-charge ratios, in the opposite order of ^{18}O labeling (Supplementary Fig. 10). In addition, the same non-simultaneous fractionation occurred in the alkaline OER (Supplementary Fig. 11). It could be assumed that the anomalous fractionation of O_2 was attributed to labeled interfacial oxygen.

Ex situ stable isotope testing of the electrolyte confirmed that the isotopic abundance was not contaminated during different stripping-

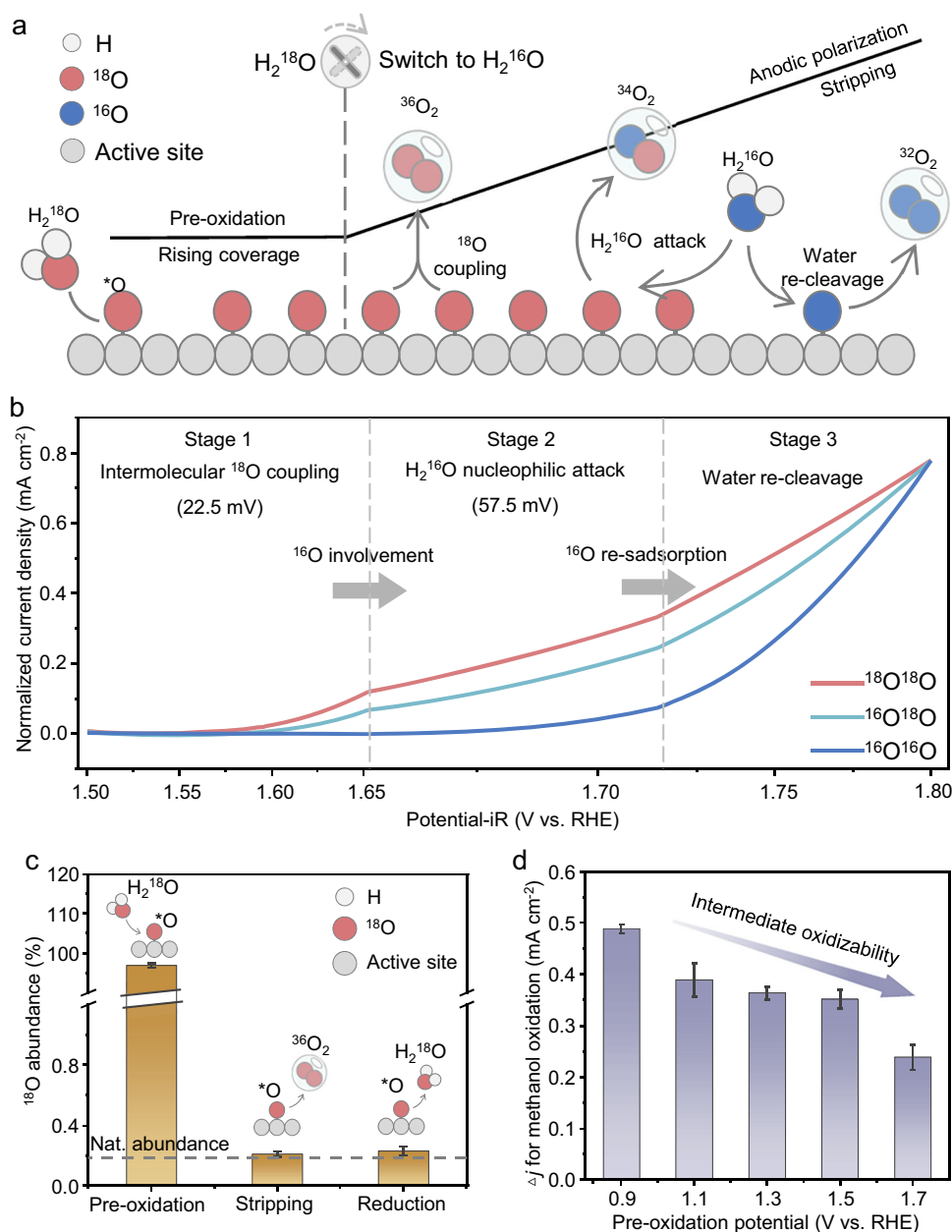


Fig. 3 | Extraordinary fractionation of O_2 induced by isotope labeling of interfacial oxygen via stripping-like voltammetry. **a** Schematic of stripping-like voltammetry for isotopic labeling of $^*\text{O}$ based on MFC-MS; **b** Normalized partial current of O_2 with $^{18}\text{O}^{18}\text{O}$, $^{16}\text{O}^{18}\text{O}$ and $^{16}\text{O}^{16}\text{O}$ during stripping-like procedure. Reaction conditions: electrolytes 0.5 M H_2SO_4 with H_2^{16}O and H_2^{18}O (pH=0); pre-oxidation potential and time 1.5 V for 180 s; stripping potential range 0.5–1.8 V; scan rate 10 mV s^{-1} . The potential was iR corrected (the uncompensated resistance: 21.13 Ω , the surface area: 0.02 cm^2); **c** Isotopic abundance of the electrolyte at different

stages during stripping-like voltammetry. Values are presented as the mean, with error bars indicating standard deviation ($n = 3$ replicates); **d** Effect of oxygen species formed by various pre-oxidation potentials on methanol oxidation. Reaction conditions: electrolytes 0.5 M H_2SO_4 with H_2^{16}O (pH=0); pre-oxidation time 240 s; stripping potential range pre-oxidation potential -1.8 V; scan rate 10 mV s^{-1} . Values are presented as the mean, with error bars indicating standard deviation ($n = 3$ replicates). Source data for the results are provided as a Source Data file.

like periods (Fig. 3c, details of the detection and calculation of abundance were given in “Methods” section.). Additionally, analysis of H_2^{16}O after ^{18}O -labeled Pt-mem reduction showed a slight increase in ^{18}O isotopic abundance, from 0.21% to 0.25%, indicating the ^{18}O loading on the interface. The gradual shrinking and eventual disappearance of the oxygen adsorption zone with increasing pre-oxidation periods implied that the loaded interfacial oxygen could be stabilized and was available for subsequent reactions (Supplementary Fig. 12). The OER rate slightly increased compared with that for untreated Pt, with a slight reduction of overpotentials, which was similar to the phenomenon observed during the stripping-like voltammetry procedure. This

suggested that only the oxygen species bonded with catalysts were responsible for anomalous fractionation.

Lattice oxygen was a promising candidate of interfacial oxygen species, and its involvement in OER was one of the most extensively studied pathways apart from AEM³². Differential electrochemical mass spectrometry (DEMS) confirmed that lattice oxygen on Pt-mem was not involved in OER, ensuring that the OER consisted only of $^*\text{O-O}^*$ and $^*\text{O-OH}$ (Supplementary Fig. 13)³³. Ex situ X-ray diffraction (XRD) indicated that Pt-mem remained in a mixed crystalline phase during polarization, and the slight oxide formation did not disturb the intrinsic OER activity (Supplementary Fig. 14). To further verify the

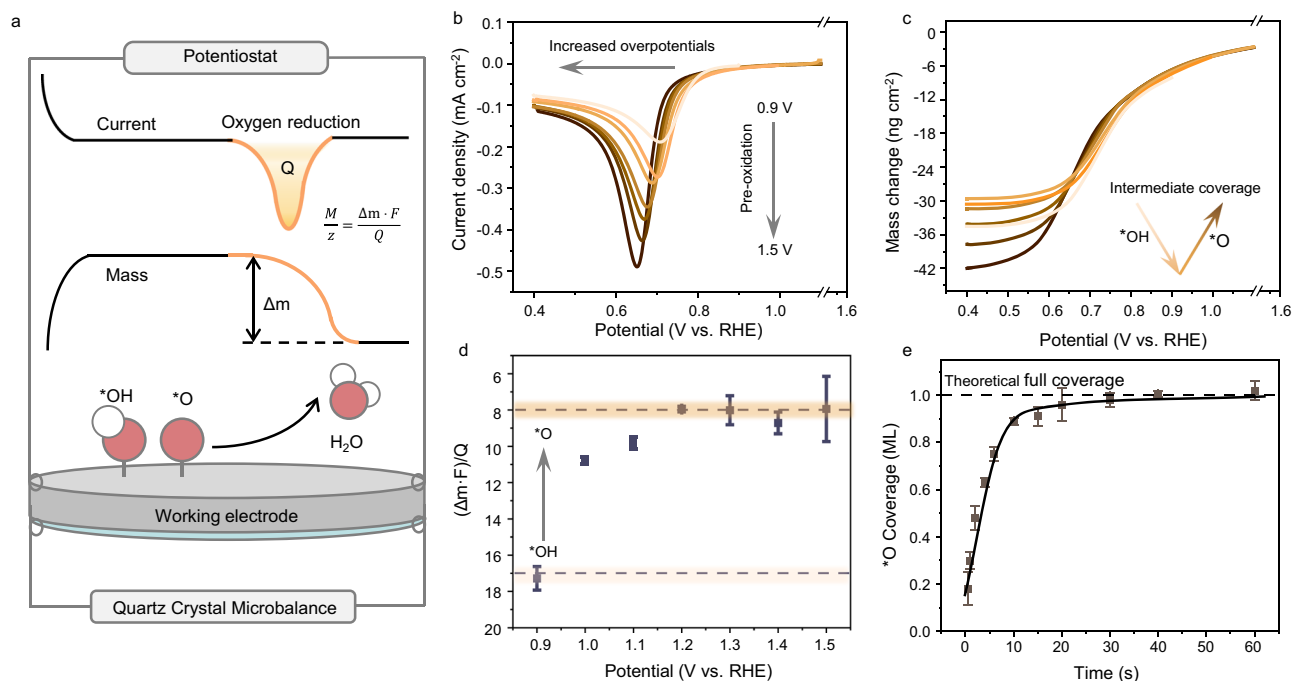


Fig. 4 | Identify the homogenized interfacial oxygen species involved in the OER. **a** Schematic of CSV for characterization of adsorbed species by EQCM; **b** Reduction peaks of oxygen species after a variety of pre-oxidation potentials; **c** Mass reduction at the interface after a variety of pre-oxidation potentials. Reaction conditions: electrolytes 0.5 M H₂SO₄ (pH=0); pre-oxidation time 60 s (reach steady state); stripping potential range pre-oxidation -0.4 V; scan rate 10 mV s⁻¹;

d Ratio of mass and electron transfer of oxygen intermediates formed at different pre-oxidation potential. Values are presented as the mean, with error bars indicating standard deviation ($n = 3$ replicates); **e** Relationship between pre-oxidation time and *O coverage of Pt-mem under 1.2 V. Values are presented as the mean, with error bars indicating standard deviation ($n = 3$ replicates). The potentials applied were no iR corrected. Source data for the results are provided as a Source Data file.

active phase, methanol, which had faster oxidation kinetics for adsorbed oxygen species such as hydroxyls (*OH), was oxidized at pre-oxidation interfaces³⁴. It displayed that after an apparent rise at 0.9 V, the kinetics of methanol oxidation decreased instead as the pre-oxidation potential grew. (Fig. 4d, and Supplementary Fig. 15). This represented a decline in the valence electrons of intermediates, that is, the oxidizing capacity³⁵. The similar activity observed among 1.1–1.5 V was probably due to the same oxygen species on the interface, whereas the reduced efficiency at higher potentials was attributed to inactivation by oxide generation. Ex situ X-ray photoelectron spectroscopy (XPS) under various potentials showed no evidence of electrooxidation to produce additional high-valence Pt oxides at low potentials, whereas visible PtO₂ formation occurred at 71.8 and 74.9 eV only after potentials above 1.5 V (Supplementary Fig. 16a)³⁶. Similarly, the O 1s spectra indicated the presence of *O, *OH, and *H₂O at 530.9, 531.8 and 533.4 eV, respectively, and weak lattice oxygen formation was detected on 529.7 eV with the rising potential (Supplementary Fig. 16b)^{37,38}. Therefore, accurate construction of homogeneous *O with specific coverages was required to connect the product distribution of OER to *O conversions.

Loading specific *O coverages by integrating mass-charge changes to profile OER based on *O conversions

The adsorbed oxygen species was identified by cathodic stripping voltammetry (CSV) on the electrochemical quartz crystal microbalance (EQCM) (Fig. 4a)³⁹. Pt quartz electrode (Pt-EQCM) exhibited an evident mass increase beginning at the oxygen adsorption region during linear sweep voltammetry (LSV) (Supplementary Fig. 17). However, the similar molecular weights between *OH and *O made it difficult to ascertain the adsorbed species based on mass change exclusively. According to CSV, the ratio of molar mass changing to electron transfer (M/z) obtained by reducing the oxygen species forming from pre-oxidation could determine the oxygen species at

various potential⁴⁰. As the pre-oxidation potential increased, the gradual negative shift of the oxygen reduction reaction (ORR) peak implied a rising oxidation state of the adsorbed species (Fig. 4b). Meanwhile, the mass change of the Pt quartz electrode showed a trend of slight decline followed by an increase (Fig. 4c). The corresponding ORR peak at its breakpoint also exhibited a more pronounced negative shift, implying a variation in intermediates species.

By calculating the mass and charge changes, the M/z of 16.92 at 0.9 V indicated that all interfacial oxygen species was *OH. As the pre-oxidation potential rose, M/z steadily decreased to around 8 at 1.2–1.5 V, suggesting *O or oxide film (PtO_x) formation (Fig. 4d). Thus, determining *O coverage requires further distinguishing it from PtO_x. The prevailing view posited that OER predominantly occurred on metal oxide surfaces^{41,42}. Formation of some non-primitive active sites (e.g., PtO_x) resulted in additional charge depletion, which presented a challenge in constructing specific *O coverages. In the case of Pt, the weak activity of the high-valent metal oxides made it instead a passivation film for limiting OER. In contrast, native Pt has been reported as the active site for OER (Supplementary Fig. 18)³⁷. Therefore, the charge used to form PtO_x was independent of the *O coverage. It has been also demonstrated that the electrooxidation of Pt starts with the formation of *OH first, and then *O. With the prolongation of the oxidation time, *O enters into the interior of Pt lattice by means of position exchange into the interior of the Pt lattice, the first layer of Pt is lifted and an inactive oxide film is formed. Therefore, when the charge of ORR is a monolayer of *O, which is 0.42 mC cm⁻², it can be assumed that all of the charge is used for *O formation. It should be noted that the current density here corresponded to the electrochemical active surface area (ECSA), which for Pt-mem was 7.14 cm² (Supplementary Fig. 19). It is possible to construct Pt interfaces with different *O coverages by adjusting the oxidation time. In order to avoid oxide film formation as much as possible, the lowest potential of 1.2 V for $M/z = 8$ was chosen as the pre-oxidation potential. When the pre-oxidation time was longer

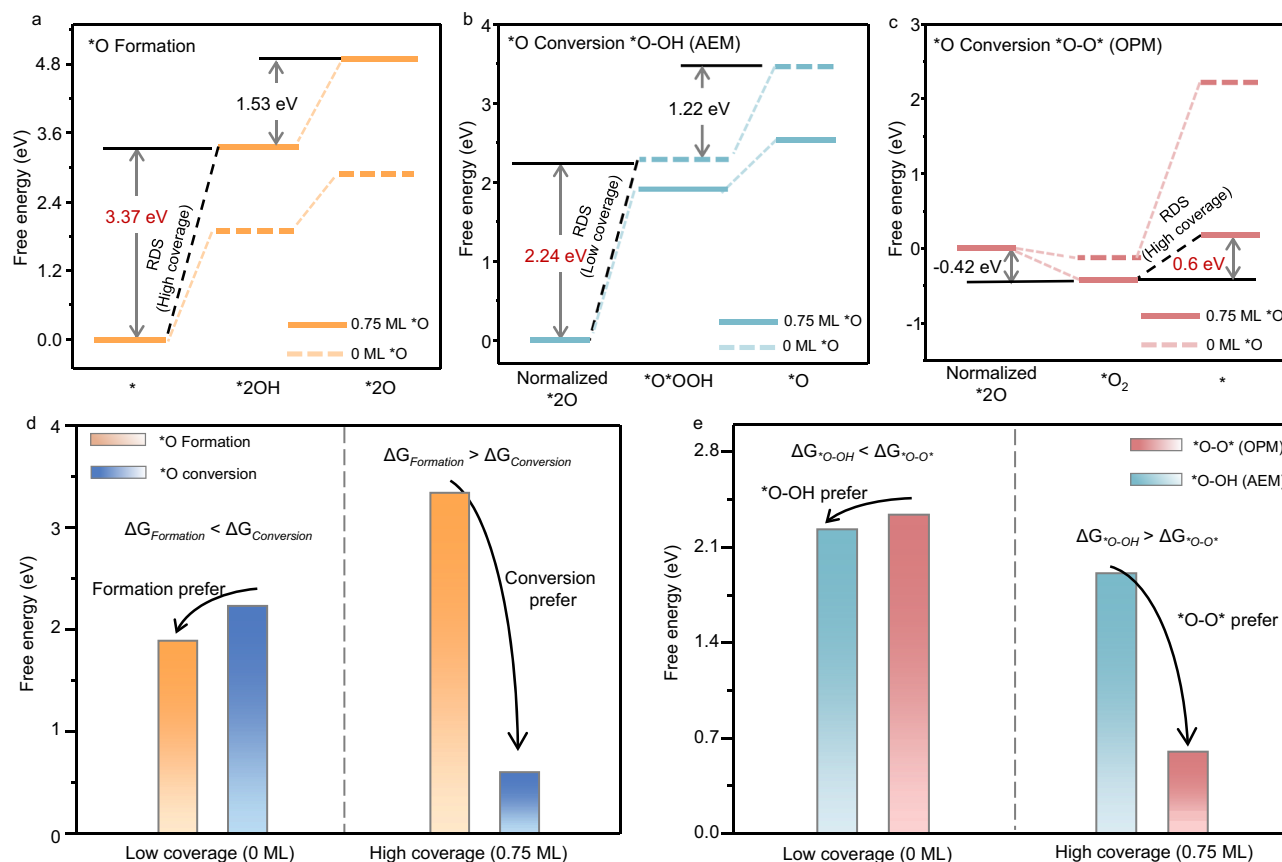


Fig. 5 | OER pathway modulation due to intermediate free energy changes induced by *O coverages. **a** ΔG of intermediates during *O formation at different coverages; **b** ΔG of intermediates during *O-OH at different coverages; **c** ΔG of

intermediates during *O-O* at different coverages; **d** The RDS of *O formation and *O conversion at high and low coverages; **e** The RDS of *O-OH and *O-O* at high and low coverages. Source data for the results are provided as a Source Data file.

than 30 s, the stripping charge reached full *O coverage and did not continue to increase obviously, indicating the formation of 1 ML *O (Supplementary Fig. 20). Establishing the relationship between pre-oxidation time and *O coverage revealed that they were inversely correlated, which provides important data for the establishment of specific *O-labeled interfaces (Fig. 4e).

Through these interfaces, it is possible to correlate the *O conversion and the partial currents of specific O_2 species. The conversions of ^{18}O and $^{32}\text{O}_2$ precipitation were not completely segregated during polarization. At potentials above the overall OER overpotential, the partial current of $^{32}\text{O}_2$ served as a marker, indicating that water re-cleavage confounded the isotopic abundance of *O. Therefore, the OER overpotential on Pt-mem was scrutinized based on *O conversions in terms of the partial currents of O_2 with different mass-to-charge ratios. First, it was known that no lattice oxygen involved in Pt-mem:

$$j_{\text{*O-O*}} + j_{\text{*O-OH}} = j_{36\text{O}_2} + j_{34\text{O}_2} + j_{32\text{O}_2} \quad (1)$$

Before the cleavage of H_2^{16}O , OER was derived entirely from labeled *O. Given that 97% H_2^{18}O was applied in this experiment, the O_2 signals with different mass-to-charge ratios had to be further deconvolved. In the case of H_2^{18}O (Supplementary Fig. 5):

$$j_{36\text{O}_2} : j_{34\text{O}_2} : j_{32\text{O}_2} = 94.090 : 5.820 : 0.090 \quad (2)$$

Because the $^{36}\text{O}_2$ signal at natural abundance is negligible, $^{36}\text{O}_2$ is exclusively triggered by *O-O*, which also consists of a trace but

irrespective amount of ^{16}O in H_2^{18}O coupling:

$$j_{\text{*O-O*}} = j_{36\text{O}_2} + 0.062j_{36\text{O}_2} + 0.001j_{36\text{O}_2} \quad (3)$$

Then, the relationship between *O-OH and oxygen signals can be readily obtained:

$$j_{\text{*O-OH}} = j_{34\text{O}_2} - 0.062j_{36\text{O}_2} \quad (4)$$

The relative contribution to the overpotential is the proportion of the partial charge obtained by integrating $j_{\text{*O-O*}}$ and $j_{\text{*O-OH}}$ to the charge that reaches 10% of the maximum total current. Considering that the *O coverage affected the water re-cleavage and thus the abundance of labeled *O, OER deconvolution was performed at different coverages. As expected, the overpotentials of *O-O* and *O-OH decreased in tandem with rising coverages, reaching 355 and 374 mV at maximum coverage, respectively (Supplementary Fig. 21a). In addition, the *O-O* contribution gradually rose with increasing coverage, peaking at 49% on 1 monolayer (ML) *O (Supplementary Fig. 21b). Scanning electron microscopy and XRD revealed that no visible morphological or structural changes occurred during the OER process, demonstrating that *O coverages also moderated the OER mechanism when aiding in the pathway dissection (Supplementary Fig. 22).

Modulation of *O conversions through regulating intermediate coverages to switch rate-determining step (RDS) of OER

To further examine the influence of coverages on analyzing *O conversions, the Gibbs free energy (ΔG) of the OER intermediates was

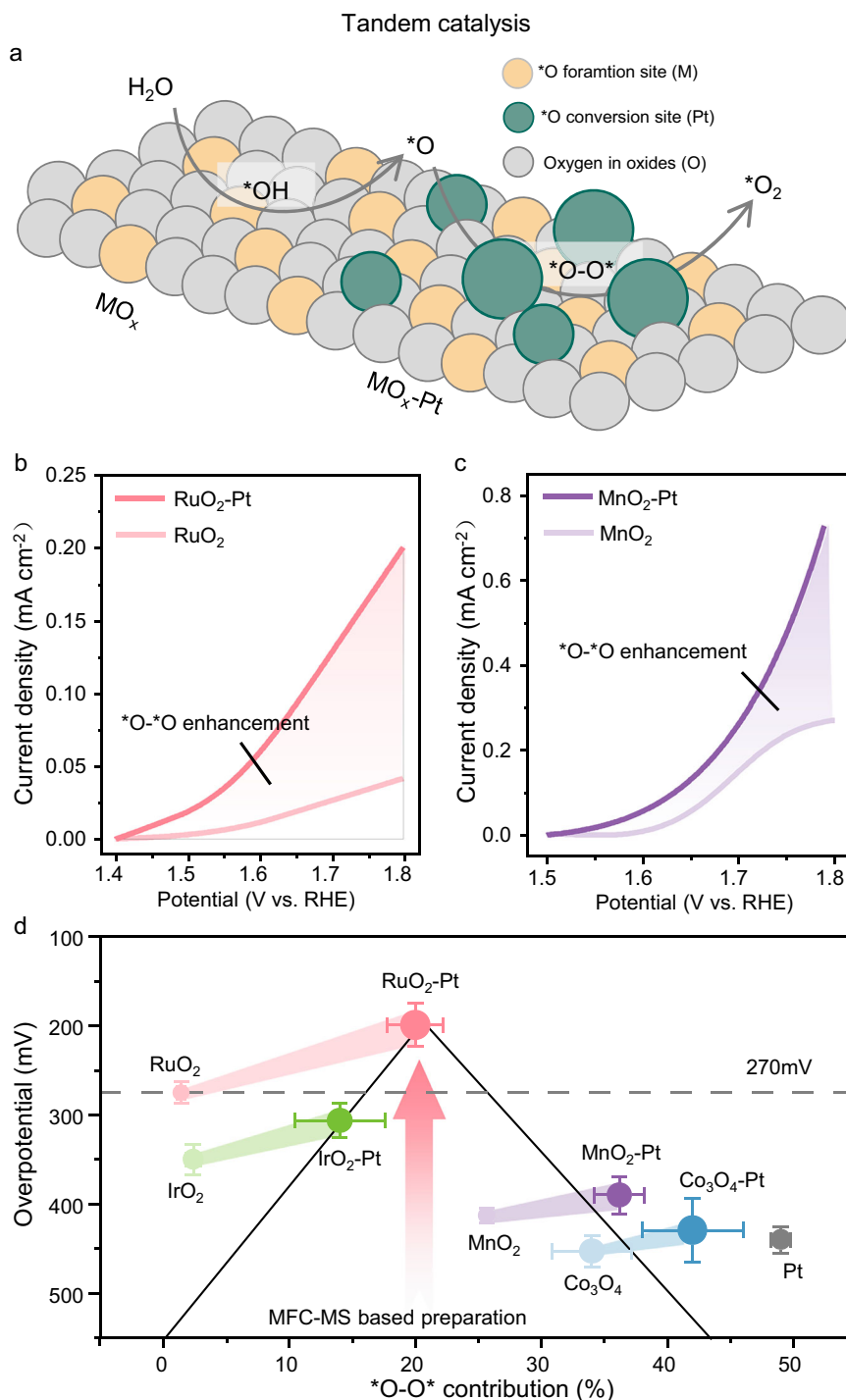


Fig. 6 | Tandem catalysts design to reduce the OER overpotential by enhancing the $^*\text{O}$ formation and conversion. **a** Schematic diagram of MO_x -Pt tandem catalysts; **b** The OER activity of RuO_2 and RuO_2 -Pt. Reaction conditions: electrolytes 0.5 M H_2SO_4 (pH=0) with H_2^{16}O and H_2^{18}O ; pre-oxidation potential and time 1.4 V for 180 s; stripping potential range pre-oxidation -1.8 V; scan rate 10 mV s^{-1} ; **c**, The OER activity of MnO_2 and MnO_2 -Pt. Reaction conditions: electrolytes 0.5 M KOH with

H_2^{16}O and H_2^{18}O (pH=13.8); pre-oxidation potential and time 1.5 V for 180 s; stripping potential range pre-oxidation -1.8 V; scan rate 10 mV s^{-1} . The potentials applied were no iR corrected; **d** Volcano plots of overpotentials and $^*\text{O}$ - $^*\text{O}$ contribution on MO_x -Pt catalysts. Values are presented as the mean, with error bars indicating standard deviation ($n = 3$ replicates). Source data for the results are provided as a Source Data file.

investigated by performing density functional theory (DFT) calculations. Since Pt-mem is a mixed crystalline phase dominated with Pt (111), calculations were performed mainly at this facet (Fig. 5, Supplementary Table 1, Supplementary Data 1). Considering that MFC-MS aimed to analyze the evolution of labeled $^*\text{O}$, the OER on Pt was divided into $^*\text{O}$ formation, namely $^*\text{O} \rightarrow ^*\text{O}_2$, and $^*\text{O}$ conversion, including $^*\text{O} \rightarrow ^*\text{O}^*\text{OOH}$ and $^*\text{O} \rightarrow ^*\text{O}_2$. At the interface without $^*\text{O}$ coverage,

the energy barrier for $^*\text{O}$ conversion was apparently higher than that for $^*\text{O}$ formation, and the relatively low $\Delta G_{^*\text{O} \rightarrow ^*\text{OOH}}$ therein as the RDS of OER demonstrated that Pt was AEM dominant during conventional polarization, in agreement with previously reported mechanisms (Fig. 5a–c, Supplementary Table 1). Furthermore, the stronger oxygen species adsorption suggested that $^*\text{OH}$ generation and dehydrogenation occurred more readily and synchronously when the applied

energy was sufficient to cause *O conversions. Thus, isotopic labeling of *O in classical in situ MS was only able to demonstrate the presence of different *O conversions due to the interference on the abundance of ^{18}O by re-cleavage of H_2O . To ensure the accuracy of the results, additional calculations performed at Pt (220) and Pt (200) exhibited a similar magnitude relationship (Supplementary Table 2, 3, Supplementary Data 1).

With the increasing *O coverage, ΔG_{OH} reached 3.36 at 0.75 ML and became the RDS of OER, in contrast to the very pronounced drop in the energy barrier for *O conversion (Fig. 5a, d). The Pt (220) and (200) surfaces demonstrate a similar trend. The difference was that ΔG_O on them became the RDS of the OER at 0.75 ML, which was the step included in *O formation (Supplementary Figs. 23a, 24a). Such a thermodynamic difference resulted in more energy being required to trigger *O generation compared to allowing labeled *O conversion. Thus, there existed a period during the polarization of the *O stripping where water re-cleavage would not occur and thus the abundance of ^{18}O was unaffected. It allowed to determine the relative contribution of different mechanisms of *O conversion to the overpotential by fractionation of O_2 .

In *O conversion process, it is noteworthy that the RDS of $^*O-O^*$ decreased more than that in $^*O-OH$, allowing the OER mechanism of Pt at high *O coverage to shift from AEM to OPM (Fig. 5b, c). This was probably due to the repulsive interactions brought by the *O coverage increase that resulted in a weakening binding between the adsorbed species to the active site. Not only did this make *O formation difficult, it also made coupling between *O coupling to each other easier, even beyond the nucleophilic attack of water (Fig. 5e). It was worth noting that the RDS of the two pathways of *O conversions did not increase monotonically with *O coverages. For $^*O-OH$, the weak binding of *O to the active site made nucleophilic attack by external water less facile. Conversely, this weak binding allowed $^*O-O^*$ spontaneous at high *O coverages, with a slight increase in the desorption energy barrier. However, this fluctuation did not affect the overall trend of the *O conversion shifting from $^*O-OH$ to $^*O-O^*$, nor did it affect the overall RDS of the OER. The same trend also appeared on the Pt (200) and (220) surfaces (Supplementary Fig. 23b, 24b). Modulating the active site spacing to enhance $^*O-O^*$ has been recognized as an effective means to break the linear scaling relationship of OER. Pt itself is not known for its OER activity because of its strong binding capacity to interfacial oxygen. Increasing the *O coverage promoted O coupling, but was accompanied by higher ΔG_{OH} and could not break the scaling relationship, resulting in a persistent high overpotential. Hence, Pt can be considered as an efficient $^*O-O^*$ metal as a promoter for conventional OER catalysts based on AEM mechanism. Constructing a tandem reaction interface relaying *O formation and $^*O-O^*$ conversion is an effective strategy to break the linear scaling relationship of the OER.

Stepwise promotion of *O formation and coupling at the tandem interface to reduce the OER overpotential

A MO_x -Pt bimetallic tandem interface was built to verify this idea. Metal oxides for different conditions, that is, RuO_2 , IrO_2 for acidic OER, MnO_2 and Co_3O_4 for alkaline conditions were used as the *O -formation interface. Pt was introduced as the $^*O-O^*$ promoter by drop-coating (Fig. 6a). The OER performance of *O -formation interfaces was evaluated by MFC-MS. RuO_2 and IrO_2 as a commonly used acidic OER catalyst exhibited high activity, predominantly with AEM, consistent with current literature (Supplementary Fig. 25, 26). On the contrary, the instability of transition metal oxides under acidic conditions led to very low activity on MnO_2 and Co_3O_4 , whereas they showed better OER properties and appreciable $^*O-O^*$ contributions in alkaline solutions (Supplementary Fig. 27, 28). It was noteworthy that both MnO_2 and Co_3O_4 show visible $^*O-O^*$ contributions under alkaline conditions, but their overpotentials were still high. It would be further discussed the relationship between the OPM mechanism and the overpotential after

the introduction of the $^*O-O^*$ promoter. The above results demonstrated that MFC-MS was applicable for OER deconvolution on any catalyst under different conditions.

As expected, RuO_2 with the $^*O-O^*$ promoter exhibited notable OER activity, with overpotentials reduced to below 200 mV. The noteworthy enhancement of $^*O-O^*$ not only broke the theoretical limit of AEM, but also rivaled the best performing OER catalysts available currently (Fig. 6b, and Supplementary Table 4). A similar phenomenon was also observed on IrO_2 , confirming the ability to reduce the OER overpotential by introducing $^*O-O^*$ promoter. On the other hand, MnO_2 with Pt sites also obtained $^*O-O^*$ enhancement and overpotential, but breaking the linear scaling relation of AEM was not achieved (Fig. 6c). It is noteworthy that, as catalysts with inherent OPM capability, both MnO_2 and Co_3O_4 did not present excellent OER activity before and after introducing $^*O-O^*$ promoter. To further explore their connection, a volcano plot of the $^*O-O^*$ contributions and the OER overpotentials was established (Fig. 6d). For the AEM-dominated interfaces, the addition of $^*O-O^*$ promoter reduced their overpotentials evidently. On the contrary, when the *O -formation interface was inherently $^*O-O^*$ -capable, further increasing the $^*O-O^*$ contribution did not help notably in overpotential reduction. This suggested the importance of balancing the *O formation and conversion rather than simply enhancing *O coupling for the design of highly active OER interfaces. Undoubtedly, emerging descriptors of the OER overpotential based on $^*O-O^*$ will be established through more detailed theoretical calculations, which may support the design of more efficient OER electrocatalysts in the future.

Discussion

In summary, by constructing isotope-labeled *O interfaces with varying levels of coverage, the overpotentials and relative contributions of different *O conversions in OER were revealed. A multi-component forced convection microchannel cell was developed to effectively control the water molecule abundance while maintaining the *O coverage. Monitored by in situ MS, the OER on interfaces with specific *O coverages was investigated through product fractionations. Although Pt had an apparent $^*O-O^*$ contribution, the weak binding energy of oxygen species still led to a high overpotential. By designing bimetallic interfaces to cascade the *O formation and conversion, it is possible to notably reduce the OER overpotential by enhancing the $^*O-O^*$ contribution. This study highlights the importance of revealing the contribution of different *O conversions for designing OER interfaces with minimal overpotential. The development of methods for tracing the conversion pathways of intermediates has great implications for the future design of high-performance electrocatalysts.

Methods

Chemicals and materials

Nanoporous PTFE membranes (20 nm pore size, uniformly distributed) were supplied by Hangzhou Cobetter Filtration Equipment Co., Ltd. Sulfuric acid (H_2SO_4 , 98%), potassium hydroxide (KOH), acetone, methanol and ethanol with the purities of 99.7% were purchased from Sinopharm Chemical Reagents Co., Ltd. (Shanghai, China). $H_2^{18}O$ (^{18}O abundance 97.3%) was purchased from Sigma-Aldrich. Pt, RuO_2 , IrO_2 , MnO_2 and Co_3O_4 with the purities of 99.9% were purchased from Sigma-Aldrich. All reagents were of analytical grade and used without further purification. The glass carbon electrodes, $HgO/HgSO_4$ electrodes (saturated K_2SO_4) and Pt wire were purchased from Shanghai Chenhua Instruments Co., Ltd. The quartz electrodes used for EQCM were purchased from Shenzhen Microbalance Technology Co., Ltd. Except for the $H_2^{18}O$ based solutions, all of others were prepared using ultrapure water (18.2 MΩ cm) (Milli-Q Advantage, Merck Millipore, Germany).

The 0.5M $H_2^{16}O$ and $H_2^{18}O$ H_2SO_4 solutions were prepared by adding, respectively, 1.36 mL and 0.136 mL of 98% H_2SO_4 to water and

diluting to final volumes of 50 mL and 5 mL. Similarly, the 0.5 M H_2^{16}O and H_2^{18}O KOH solutions were made by dissolving 1.4 g and 0.14 g of KOH in water and bringing each to a final volume of 50 mL and 5 mL. The H_2^{16}O solutions were prepared several days in advance and stored in sealed, light-protected containers, while the H_2^{18}O solutions were freshly prepared on site.

Microfluidic electrochemical cell

A microfluidic electrochemical cell was constructed with a customized chip, which was manufactured by photolithography (PL) process, including following steps: 1. Bonding the glass slide 1 and monocrystalline silicon wafer; 2. PL mask design and manufacturing; 3. spin-coating negative photoresist onto the silicon wafer; 4. mask aligning for patterning with UV light; 5. remove uncured photoresist by developer to form etching pattern; 6. wet etching of monocrystalline silicon wafer using KOH; 7. laser perforation of glass slide 2; 8. Bonding the parts from step 6 and step 7 (Fig. 1a). In detail, the glass slide 1 and the monocrystalline silicon wafer were cleaned with acetone, alcohol and pure water, respectively, and then dried under nitrogen flow. Using the glass slide as the negative pole and the silicon wafer as the positive pole, which were tightly pasted together to form a circuit. At 300–500°C, the metal ions in the glass slide moved toward the positive side under the high voltage, resulting in negative and positive charges enrichment on the glass and the silicon wafer side, respectively. The positive and negative charges were combined by electrostatic attraction, which promoted the oxidation of silicon by dissociated oxygen ions from the glass slide, resulting in extremely high bond strength. Negative photoresists were spin-coated onto silicon wafers at 3000 rpm and then baked at 100°C for 1.5 min. The PL mask ordered from the vendor was tightly fitted to the photoresist-coated wafer and exposed under UV. Because of the negative photoresist, the photoresist was cured in the area where UV light passed through. The uncured photoresist on the wafer was removed with developer to form an etching pattern. Single crystal silicon was etched using KOH until the glass sheet layer was exposed. The glass slide 2 was laser-punched with two holes of 1 mm internal diameter to serve as the liquid inlet and outlet. The etched slide 1 and slide 2 were bonded to form a glass-silicon-glass sandwich structure by anodic bonding as described above. Its dimensions are 5 mm (W) × 20 mm (L) × 2.5 mm (H), with an open cavity of 5 mm (W) × 6 mm (L) × 0.5 mm (H) and fluid inlet/outlet, which is assembled as a cell sealing by parallel working and counter electrodes. The exposed geometric surface area of the electrodes is ~0.025 cm². The working electrode potential was referenced against an HgO/HgSO₄ electrode upstream of the cell that was calibrated against a homemade standard hydrogen electrode. PEEK fixtures are used to hold the membrane electrodes in place, and copper conductive tape is applied for electrical contact. Multi-channel syringe pump pushes different fluids programmatically into the chip through a programmable logic controller to construct the electrode interface.

MFC-MS system

Volatile species produced on electrode interface is drawn downward through the PTFE membrane by pressure difference for mass spectrometry analysis. The microfluidic electrochemical cell is connected to the mass spectrometer via a capillary in the PEEK fixture behind the working electrode. The PEEK fixture remains completely sealed except for the injection port, which creates a vacuum chamber for product capture and analysis during testing. To prevent potential damage to the mass spectrometer, a cold trap cooled by dry ice is required, serving to condense and remove water vapor before it reaches the instrument. The mass spectrometer features two connected vacuum chambers: one is the main chamber maintained at high vacuum, and the other is a secondary chamber with a lower vacuum level, which is directly linked to the microfluidic electrochemical cell operating under ambient pressure. When the OER tests were performed in MFC-MS

system, Pt-mem or the (bimetallic) catalyst loaded on Au-coated PTFE membrane served as the working electrode, HgO/HgSO₄ as the reference electrode, and Pt-mem as the counter electrode. The compartment volume was 0.015 mL.

Preparation of membrane electrodes

A nanoporous PTFE membrane (20 nm pore size) was used as the pervaporation membrane and electrocatalyst support. It was sonicated in acetone for 30 min, sonicated in methanol for 30 min, rinsed with DI water, dried over N₂, and exposed to UV generated ozone for 5 min to clean the surface prior to sputter deposition. Pt (99.999%) was deposited onto the nanoporous PTFE membrane using the CIS400 magnetron ion sputtering instrument (Shanghai Zhongbin Technology Co., Ltd) to form Pt-mem with an effective thickness of 400 nm. Au (99.999%) was deposited onto the PTFE membrane with 400 nm thickness to form the membrane electrode carrier for other catalysts. In the MFC-MS system, the exposed geometric area was 0.02 cm². In DEMS system, the exposed geometric area was 1.77 cm².

Preparation of Pt, metal oxides and bimetallic electrodes

Pt powder, RuO₂, IrO₂, MnO₂ and Co₃O₄ were commercially available. The catalyst ink was prepared by dispersing Pt and the metal oxides (4 mg) were dispersed in a mixture of 1.5 mL of deionized water and ethanol with a volume ratio of 4:1, with 40 μL of Nafion solution as a binder. After ultrasonication for 1 h, 6 μL of homogeneous ink was dropped on glassy carbon (geometric area 0.07 cm²) and Au-coated PTFE membrane (geometric area 0.02 cm²) and fully dried in air at room temperature. The mass loadings of the electrocatalysts onto two types of electrodes were controlled at ~4 mg/1.5 mL × 0.006 mL/0.07 cm² = 0.23 mg cm⁻² and 4 mg/1.5 mL × 0.006 mL/0.02 cm² = 0.80 mg cm⁻², respectively. As for bimetallic interfaces, 3 μL of the metal oxide was dropped on electrodes firstly. After drying, 3 μL of Pt was added to ensure the same loadings on two types of electrodes. The mass loading of each metal (oxide) was 0.11 and 0.40 mg cm⁻², respectively.

Electrochemical measurements of OER

The OER measurements were evaluated with in situ MS, EQCM and a standard three-electrode cell, respectively, equipped with CHI 660E electrochemistry workstation (Chenhua, Shanghai). Except for cells used for in situ characterization, a HgO/HgSO₄ electrode (saturated K₂SO₄) and Pt wire were employed as the reference and counter electrode, respectively. Under acidic conditions, the electrolyte is 0.5 M H₂SO₄ (pH=0.2 ± 0.02). Under alkaline conditions, the electrolyte is 0.5 M KOH (pH=13.8 ± 0.04). The potentials from HgO/HgSO₄ to the RHE scale was performed using the following equation:

$$E_{\text{RHE}} = E_{\text{HgO/HgSO}_4} + 0.0591 \times \text{pH} + 0.64 \quad (5)$$

The HgO/HgSO₄ reference electrode was calibrated by following method: In H₂-saturated 0.5 M H₂SO₄ electrolyte (pH=0), two Pt wires were used as working and counter electrodes. CV was conducted over a potential range of -0.75 V to -0.55 V at a scan rate of 1 mV s⁻¹ to maintain equilibrium conditions. The calibrated potential of the reference electrode was determined by averaging the two electrode potentials corresponding to the zero current density point. In MFC-MS system, potential tests on Pt-mem were additional corrected by iR drop due to uncompensated resistance, which was found to be 21.13 ± 0.22 Ω when the voltage waveforms were centered at increasingly anodic potentials. In this research, the extremely small current generated by the sufficiently small electrode area (0.02 cm²) has a negligible impact on the determination of overpotential (Supplementary Fig. 29). Therefore, except for the Pt-mem tests in MFC-MS, the potentials measured in other systems were not iR-compensated.

CV with a scanning rate of 10 mV s⁻¹ was measured in the potential range of 0.4–1.8 V vs. RHE. LSV was performed in the potential range of 1.2–1.8 V vs. RHE at a scanning rate of 10 mV s⁻¹. If not specified, all current densities are geometric current densities (geometric surface area: MFC-MS = 0.02 cm², DEMS = 1.77 cm², EQCM = 0.20 cm², and glassy carbon electrode = 0.07 cm²). The partial currents of molecular oxygen from different isotopes were obtained through the linear relationship between the Faradic currents and ion currents constructed by steady state measurements. The MFC-OER derived OER overpotentials and onset potentials were evaluated as the electrode potential at which the currents reached 10% and 1% of its maximum, respectively. The relative contribution to the overpotential was the proportion of the partial charge obtained by integrating partial currents to the charge that reached 10% of the maximum total current.

Unless otherwise specified, all current densities are geometric current densities (MFC-MS 0.02 cm², DEMS 1.77 cm², EQCM 0.20 cm², and glassy carbon electrode 0.07 cm²). The partial current of molecular oxygen from different isotopes was obtained through in situ MS to measure the ionic current, which was then converted using the linear relationship between O₂ and current obtained from steady-state measurements.

Kinetic isotope effect (KIE)

According to previous literature, KIE was estimated via multicycles chronoamperometric tests, which carried out in 0.5 M H₂SO₄ with H₂¹⁶O and H₂¹⁸O. The KIE value was calculated from the following equation:

$$\text{KIE} = \frac{J_{\text{H}_2^{16}\text{O}}}{J_{\text{H}_2^{18}\text{O}}} \quad (6)$$

Where $J_{\text{H}_2^{16}\text{O}}$ and $J_{\text{H}_2^{18}\text{O}}$ are the average current density in H₂¹⁶O and H₂¹⁸O under 1.7 V, respectively. The average current density values of multicycles were linear fitted. The KIE value was estimated from the ratio of the two data points in the two fitted line in H₂¹⁶O and H₂¹⁸O.

Differential electrochemical mass spectrometry (DEMS)

DEMS system was employed in our previous studies. The electrochemical cell is a typical three-electrode system with a volume of around 2 mL. The small volume is suitable for isotope experiments. Pt-mem was employed as the working electrode, while a HgO/HgSO₄ electrode (saturated K₂SO₄) and Pt wire were the reference and counter electrode, respectively. The pressure difference allows the in situ generated O₂ to be drawn downward into the vacuum chamber for mass spectrometer analysis instead of being released upward into the air. Pt-mem was polarized in 0.5 M H₂SO₄ (pH=0) prepared with H₂¹⁶O and H₂¹⁸O as solvents, respectively, at a scan rate of 10 mV s⁻¹ in the 0.4–1.7 V potential range to determine the O₂ fractionation at different isotopic abundances.

For isotopic labeling studies, constant potential electrolysis in H₂¹⁸O solvent at 1.8 V was performed to isotopically label the catalyst surface. The catalyst was then washed with H₂¹⁶O and dried to remove adsorbed oxygen and water from the catalyst layer, while ¹⁸O lattice oxygen was retained. Subsequent LSV of Pt-mem with H₂SO₄ in H₂¹⁶O solvent was tested to monitor the fractionation of O₂.

Isotope ratio mass spectrometry (IRMS)

Considering that the volume of the microfluidic electrochemical cell is about 20 μL, it was chosen as the sample volume to analyze the isotope abundance of the liquid-phase interface at different stages. To ensure the accuracy of the IRMS analysis, the electrolyte was fed directly into the dry ice cooling trap via a microtube. The corresponding solidified electrolyte was intercepted according to the different stages of the reaction to ensure that it was not contaminated. The abundance of

isotopes measured by IRMS is usually expressed by δ :

$$\delta^{18}\text{O}(\%) = \left(\frac{R_{\text{SQ}}}{R_{\text{St}}} - 1 \right) \times 100 \quad (7)$$

where R_{SQ} is the isotope ratio of the sample and R_{St} (0.002) is the isotope ratio of the standard:

$$R = \frac{{}^{18}\text{O}}{{}^{16}\text{O}} \quad (8)$$

As for ¹⁸O abundance, ¹⁷O is negligible:

$$\text{Abundance} = \frac{{}^{18}\text{O}}{{}^{16}\text{O} + {}^{18}\text{O}} = \frac{R_{\text{SQ}}}{R_{\text{SQ}} + 1} \quad (9)$$

Electrode characterization

The electrode morphology of the Pt-mem was acquired using a field emission scanning electron microscope (ZEISS Merlin Compact; Jena; Germany). The bulk crystal structures of Pt-mem was analyzed using a D8 Advance X-ray diffractometer (Bruker; Karlsruhe; Germany) using Cu K α radiation. The near-surface compositions and surface oxygen adsorbates of the Pt-mem was measured using a Thermo Scientific K-Alpha X-ray photoelectron spectrometer.

Electrochemical quartz crystal microbalance (EQCM) test

All EQCM measurements were performed using CHI 440 C (Chenhua; Shanghai). The three-electrode EQCM setup was applied with Pt-coated quartz crystals (geometric area 0.2 cm², basic oscillating frequency of 7.995 MHz) as working electrodes, the platinum wire functioned as counter electrode, and Hg/HgSO₄ was employed as reference electrode. The EQCM measurements were interpreted based on the Sauerbrey equation:

$$\Delta f = - \frac{2f_0^2 \Delta m}{A \sqrt{\rho_q \mu_q}} \quad (10)$$

where Δf represented the resonant frequency change, and Δm stood for the mass change of electrodes. f_0 denoted the basic oscillating frequency. A was the geometric area of the electrode. ρ_q and μ_q were the density (2.648 g cm⁻³) and shear modulus (2.947 × 10¹¹ g cm⁻¹ s⁻²) of the quartz crystal, respectively. To achieve reliable and repeatable electrochemical behavior, initial conditioning cycles were conducted before recording EQCM data. To determine the molecular weight using the ratio of Δm to ΔQ , the Faraday's law was utilized:

$$Q = n \times F \times z \quad (11)$$

$$Q = \frac{\Delta m}{M} \times F \times z \quad (12)$$

$$\frac{M}{z} = \frac{\Delta m \cdot F}{Q} \quad (13)$$

where the charge Q was the integral of the current variation with time, n represented the mole number, M was the molecular weight of species, z is the number of electron transfer (*OH is 1, *O is 2), F is the Faraday constant (96485 C mol⁻¹).

Finite element simulations

The fluid motions inside the cell were all simulated in Fluent software using the Mixture multi-phase flow model. The fluxes of different

phases entering the grid per unit time were weighted and averaged to obtain the macroscopic fluid motion trend in that grid for transfer, realizing the velocity, density, pressure, and other physical quantities of different fluid phases for solving the calculations. Considering the very low Reynolds number of the flow, Laminar flow model was used for the calculation. A transient pressure-based solver was used to perform the calculations with second-order wind-type accuracy by means of a transient coupled-type algorithm. For the simulation of the fluid replacement process within the cell, due to the similarity of density, viscosity between the two liquids, no surface tension between the phases, and no clear cross-interface after mixing, the surface tension coefficient was 0 nm^{-1} with the volumetric force format.

DFT calculations

DFT calculations were carried out using the Vienna Ab initio simulation package (VASP) in all calculations. The generalized gradient approximation of Perdew-Burke-Ernzerhof (GGA-PBE) was employed to describe the exchange-correlation potential. The interactions between ion cores and valence electrons were handled by the projector augmented-wave (PAW) method. The energy of plane-wave cutoff was kept at 400 eV. Structural relaxation was proceeded until the Hellmann-Feynman forces fell below -0.03 eV/\AA and the total energy change was less than 10^{-5} eV . In all adsorption models, the dispersion interactions among atoms was described by Grimme's DFT-D3 methodology. The Brillouin zone k-points were set as $3 \times 3 \times 1$ because the energies converged when they were larger than $2 \times 2 \times 1$. (Supplementary Fig. 29). The catalytic surfaces adopted the Pt (111), (220) and (200) crystal plane models constructed by five layers of Pt atoms. The supercell sizes of Pt (111), (220) and (200) were $11.08 \times 11.08 \times 24.05 \text{ \AA}^3$, $15.70 \times 11.08 \times 20.55 \text{ \AA}^3$ and $11.08 \times 11.08 \times 22.85 \text{ \AA}^3$ (containing 80 Pt atoms), respectively. The bottom two layers of atoms on all models were fixed. Set a 15 \AA vacuum layer along the normal direction of the surface (Z-axis) and enable dipole correction to eliminate the periodic boundary effect. The reaction intermediates ($^*2 \text{ OH}$, $^*2\text{O}$, $^*\text{O}^*\text{OOH}$, $^*\text{O}$, and $^*\text{O}_2$) were placed at the characteristic adsorption sites: $^*\text{OH}$ was preferentially adsorbed at the top position, $^*\text{O}$ occupied the triple hole position, and $^*\text{O}_2$ and $^*\text{OOH}$ were located at the bridge position. The multi-adsorption system maintained a minimum spacing of $>4 \text{ \AA}$ to avoid false interactions. In the $0.375 \text{ ML } ^*\text{O}$ -covered Pt system, the magnetic moments of the four initial O atoms were 0.019, 0.020, 0.020, and 0.019 μB , respectively, all close to 0.02 μB (well below the threshold of 0.1 μB). This indicated that spin polarization had an extremely weak effect on the electronic structure. Therefore, all systems were treated as closed shells (ISPIN = 1). The Gibbs free energy change was defined as:

$$\Delta G = \Delta E + \Delta \text{ZPE} - T\Delta S \quad (14)$$

where ΔE was the electronic energy calculated with VASP, ΔZPE (zero point energy correction) and ΔS (entropy change) were obtained through the calculation of vibration frequency at the temperature $T = 298.15 \text{ K}$. In particular, entropic contributions of H_2 and H_2O included translational/rotational/vibration entropy, obtained from NIST database and literature (Supplementary Table S)^{43–45}.

Data availability

The data generated in this study are provided in the Source Data file. Coordinates of the optimized DFT models is provided as Supplementary Data. The data used in this study are available in the Figshare database under accession code <https://doi.org/10.6084/m9.figshare.29631899>. Source data are provided with this paper.

References

- Birdja, Y. Y. et al. Advances and challenges in understanding the electrocatalytic conversion of carbon dioxide to fuels. *Nat. Energy* **4**, 732–745 (2019).
- Jiao, Y., Zheng, Y., Jaroniec, M. & Qiao, S. Z. Design of electrocatalysts for oxygen- and hydrogen-involving energy conversion reactions. *Chem. Soc. Rev.* **44**, 2060–2086 (2015).
- Tong, W. et al. Electrolysis of low-grade and saline surface water. *Nat. Energy* **5**, 367–377 (2020).
- John, J., MacFarlane, D. R. & Simonov, A. N. The why and how of NO_x electroreduction to ammonia. *Nat. Catal.* **6**, 1125–1130 (2023).
- Zhao, Y. et al. Oxygen evolution/reduction reaction catalysts: from in situ monitoring and reaction mechanisms to rational design. *Chem. Rev.* **123**, 6257–6358 (2023).
- Chatenet, M. et al. Water electrolysis: from textbook knowledge to the latest scientific strategies and industrial developments. *Chem. Soc. Rev.* **51**, 4583–4762 (2022).
- Okamura, M. et al. A pentanuclear iron catalyst designed for water oxidation. *Nature* **530**, 465–468 (2016).
- Lin, C. et al. In-situ reconstructed Ru atom array on $\alpha\text{-MnO}_2$ with enhanced performance for acidic water oxidation. *Nat. Catal.* **4**, 1012–1023 (2021).
- Huang, Z.-F. et al. Strategies to break the scaling relation toward enhanced oxygen electrocatalysis. *Matter* **1**, 1494–1518 (2019).
- Kodera, M. et al. Reversible O–O bond scission of peroxodiiron(III) to high-spin oxodiiron(IV) in dioxygen activation of a diiron center with a bis-tpa dinucleating ligand as a soluble methane monooxygenase model. *J. Am. Chem. Soc.* **134**, 13236–13239 (2012).
- Yang, S. et al. The mechanism of water oxidation using transition metal-based heterogeneous electrocatalysts. *Chem. Soc. Rev.* **53**, 5593–5625 (2024).
- Ren, H. et al. Operando proton-transfer-reaction time-of-flight mass spectrometry of carbon dioxide reduction electrocatalysis. *Nat. Catal.* **5**, 1169–1179 (2022).
- Song, H. et al. $\text{RuO}_2\text{-CeO}_2$ lattice matching strategy enables robust water oxidation electrocatalysis in acidic media via two distinct oxygen evolution mechanisms. *ACS Catal.* **14**, 3298–3307 (2024).
- Oener, S. Z., Bergmann, A. & Cuenya, B. R. Designing active oxides for a durable oxygen evolution reaction. *Nat. Synth.* **2**, 817–827 (2023).
- Lee, S., Banjac, K., Lingenfelder, M. & Hu, X. Oxygen isotope labeling experiments reveal different reaction sites for the oxygen evolution reaction on nickel and nickel iron oxides. *Angew. Chem. Int. Ed.* **58**, 10295–10299 (2019).
- Scott, S. B. et al. The low overpotential regime of acidic water oxidation part I: the importance of O_2 detection. *Energy Environ. Sci.* **15**, 1977–1987 (2022).
- Yang, Y.-Y. et al. Electrocatalysis of ethanol on a Pd electrode in alkaline media: an in situ attenuated total reflection surface-enhanced infrared absorption spectroscopy study. *ACS Catal.* **4**, 798–803 (2014).
- Hasa, B., Jouny, M., Ko, B. H., Xu, B. & Jiao, F. Flow electrolyzer mass spectrometry with a gas-diffusion electrode design. *Angew. Chem. Int. Ed. Engl.* **60**, 3277–3282 (2021).
- Ye, K. et al. Resolving local reaction environment toward an optimized CO_2 -to- CO conversion performance. *Energy Environ. Sci.* **15**, 749–759 (2022).
- Clark, E. L. & Bell, A. T. Direct Observation of the local reaction environment during the electrochemical reduction of CO_2 . *J. Am. Chem. Soc.* **140**, 7012–7020 (2018).
- Chang, J. et al. Oxygen radical coupling on short-range ordered Ru atom arrays enables exceptional activity and stability for acidic water oxidation. *J. Am. Chem. Soc.* **146**, 12958–12968 (2024).
- Rao, R. R. et al. Operando identification of site-dependent water oxidation activity on ruthenium dioxide single-crystal surfaces. *Nat. Catal.* **3**, 516–525 (2020).
- Liang, C. et al. Unravelling the effects of active site density and energetics on the water oxidation activity of iridium oxides. *Nat. Catal.* **7**, 763–775 (2024).

24. Li, J. et al. Weak CO binding sites induced by Cu–Ag interfaces promote CO electroreduction to multi-carbon liquid products. *Nat. Commun.* **14**, 698 (2023).
25. Lu, S.-M. et al. Hydrodynamics-controlled single-particle electrocatalysis. *J. Am. Chem. Soc.* **146**, 15053–15060 (2024).
26. Ma, M. C., Li, G., Chen, X., Archer, L. A. & Wan, J. Suppression of dendrite growth by cross-flow in microfluidics. *Sci. Adv.* **7**, eabf6941 (2021).
27. Ibrahim, O. A. et al. Microfluidics for electrochemical energy conversion. *Chem. Rev.* **122**, 7236–7266 (2022).
28. Reier, T., Oezaslan, M. & Strasser, P. Electrocatalytic oxygen evolution reaction (OER) on Ru, Ir, and Pt catalysts: a comparative study of nanoparticles and bulk materials. *ACS Catal.* **2**, 1765–1772 (2012).
29. Yang, Y. et al. Inverse kinetic isotope effects in the oxygen reduction reaction at platinum single crystals. *Nat. Chem.* **15**, 271–277 (2023).
30. Du, K. et al. Interface engineering breaks both stability and activity limits of RuO₂ for sustainable water oxidation. *Nat. Commun.* **13**, 5448 (2022).
31. Huang, J. et al. Modifying redox properties and local bonding of Co₃O₄ by CeO₂ enhances oxygen evolution catalysis in acid. *Nat. Commun.* **12**, 3036 (2021).
32. Grimaud, A. et al. Activating lattice oxygen redox reactions in metal oxides to catalyse oxygen evolution. *Nat. Chem.* **9**, 457–465 (2017).
33. Amin, H. M. A., Königshoven, P., Hegemann, M. & Baltruschat, H. Role of lattice oxygen in the oxygen evolution reaction on Co₃O₄: isotope exchange determined using a small-volume differential electrochemical mass spectrometry cell design. *Anal. Chem.* **91**, 12653–12660 (2019).
34. Li, L. et al. Lanthanide-regulating Ru–O covalency optimizes acidic oxygen evolution electrocatalysis. *Nat. Commun.* **15**, 4974 (2024).
35. Tao, H. B. et al. A general method to probe oxygen evolution intermediates at operating conditions. *Joule* **3**, 1498–1509 (2019).
36. Kötze, R., Lewerenz, H. J. & Stucki, S. XPS Studies of oxygen evolution on Ru and RuO₂ anodes. *J. Electrochem. Soc.* **130**, 825 (1983).
37. Favaro, M. et al. Elucidating the alkaline oxygen evolution reaction mechanism on platinum. *J. Mater. Chem. A* **5**, 11634–11643 (2017).
38. Arrigo, R. et al. In situ study of the gas-phase electrolysis of water on platinum by NAP-XPS. *Angew. Chem. Int. Ed.* **52**, 11660–11664 (2013).
39. Bucur, R. V. The resting-state of the Pt-black electrode in acid solution and the structure of the adsorption layer. Coulometric and electrochemical quartz crystal microbalance measurements. *Electrochim. Acta* **62**, 354–361 (2012).
40. Mathew, P., Meyers, J. P., Srivastava, R. & Strasser, P. Analysis of surface oxidation on Pt and Pt core-shell electrocatalysts for PEFCs. *J. Electrochem. Soc.* **159**, B554 (2012).
41. Huang, J., Scott, S. B., Chorkendorff, I. & Wen, Z. Online electrochemistry–mass spectrometry evaluation of the acidic oxygen evolution reaction at supported catalysts. *ACS Catal.* **11**, 12745–12753 (2021).
42. Rossmeisl, J., Qu, Z. W., Zhu, H., Kroes, G. J. & Nørskov, J. K. Electrolysis of water on oxide surfaces. *J. Electroanal. Chem.* **607**, 83–89 (2007).
43. Viswanathan, V., Hansen, H. A. & Nørskov, J. K. Selective electrochemical generation of hydrogen peroxide from water oxidation. *J. Phys. Chem. Lett.* **6**, 4224–4228 (2015).
44. Nørskov, J. K. et al. Trends in the exchange current for hydrogen evolution. *J. Electrochem. Soc.* **152**, J23–J26 (2005).
45. Yang, T. T. & Saidi, W. A. The Bell-Evans-Polanyi relation for hydrogen evolution reaction from first-principles. *npj Comput. Mater.* **10**, 98 (2024).

Acknowledgements

This research is financially supported by National Natural Science Foundation of China (22276138), National Key Research and Development Program of China (2023YFC3711100) and the Fundamental Research Funds for the Central Universities (2022-4-ZD-07) from Y. W.

Author contributions

Y. W. supervised the project and designed the study. Z. C. conceived the key ideas and electrolytic reactor. Z. C. and X. Z. carried out the electrochemical experiments and data analysis. Z. L. synthesized and characterized the catalysts. Y. L. performed the computational analysis. Y. W., Z. C. and Y. L. provided input on manuscript editing and discussions. All authors contributed to data interpretation and manuscript revision.

Competing interests

The authors declare no competing interests.

Additional information

Supplementary information The online version contains supplementary material available at <https://doi.org/10.1038/s41467-025-63181-z>.

Correspondence and requests for materials should be addressed to Ying Wang.

Peer review information *Nature Communications* thanks Luis Ruiz and the other anonymous reviewer(s) for their contribution to the peer review of this work. A peer review file is available.

Reprints and permissions information is available at <http://www.nature.com/reprints>

Publisher's note Springer Nature remains neutral with regard to jurisdictional claims in published maps and institutional affiliations.

Open Access This article is licensed under a Creative Commons Attribution-NonCommercial-NoDerivatives 4.0 International License, which permits any non-commercial use, sharing, distribution and reproduction in any medium or format, as long as you give appropriate credit to the original author(s) and the source, provide a link to the Creative Commons licence, and indicate if you modified the licensed material. You do not have permission under this licence to share adapted material derived from this article or parts of it. The images or other third party material in this article are included in the article's Creative Commons licence, unless indicated otherwise in a credit line to the material. If material is not included in the article's Creative Commons licence and your intended use is not permitted by statutory regulation or exceeds the permitted use, you will need to obtain permission directly from the copyright holder. To view a copy of this licence, visit <http://creativecommons.org/licenses/by-nc-nd/4.0/>.

© The Author(s) 2025